Characteristics of two-azimuth seismic ionospheric disturbances following the 2020 Jamaica earthquake from GPS observations

Yi Chai [1, 2], Shuanggen Jin [1, 3*]

[1] Shanghai Astronomical Observatory, Chinese Academy of Sciences, Shanghai 200030, China

[2] University of Chinese Academy of Sciences, Beijing 100047, China

[3] School of Remote Sensing and Geomatics Engineering, Nanjing University of Information Science and Technology, Nanjing 210044, China

Abstract: Earthquakes often occur and may induce the ionospheric disturbance. In order to understand the generation and process of the earthquake, the seismic ionospheric disturbance (SID) may provide insights on earthquakes. In this paper, the seismic ionospheric disturbances following the Mw 7.7 Jamaica earthquake on 28 January 2020 are detected after 12min of the main shock by the dual-frequency GPS measurements. Two disturbances in different azimuths are significantly found by satellite PRN26 and PRN03. The one is located at the southwest area in the range of 700-800km away from the epicenter while the other is located at the southeast area in the range of 200-450km. The propagation speeds of the two disturbances are 2.53km/s and 2.57km/s respectively. Furthermore, we estimated the detailed characteristics of SID (primarily the amplitude, elevation and azimuth angle, waveform and frequency) and discussed the generation and motion process of the ionospheric disturbance with seismograph, focal mechanism and magnetic field. The relation among SID, Rayleigh wave and focal mechanism are interpreted. Furthermore, the azimuthal asymmetry of SID amplitude and the appearance of the inverted N-shape waveform observed by satellite PRN26 are the main distinctions in the two disturbances as a result. Finally, the up propagating secondary acoustic wave triggered by the seismic Rayleigh wave from the strike-slip earthquake is the main source of the two disturbances.

Keywords: seismic ionospheric disturbance (SID); GPS; Rayleigh wave; strike-slip earthquake

1. Introduction

Earthquakes are common natural disasters. During the main shock of an earthquake, the earthquake rupture and severe co-seismic vertical crust movements can excite acoustic resonance, and some of the acoustic resonance can propagate upward into the ionosphere in

the form of acoustic waves and induce variations of the ionospheric electron density which is the so-called ionospheric disturbances. In short, the ionospheric disturbances relate to the acoustic-gravity wave launched by big earthquake [1,2]. The first ionosphere disturbance was detected by ionospheric vertical sounding following the great Alaska earthquake in 1964 [3]. And the frequency oscillations in radio signals follow the Alaska were detected in the same earthquake [4]. Since then, the researches for seismic ionospheric disturbance (SID) have attracted great attention and made contributions to reveal the mechanism of earthquake motion and crust vertical movement.

However, as the limitation of the measurement instruments in last few decades, there are difficulties in studying the more detailed characteristics of ionospheric disturbance. Nowadays, dense Global Position System (GPS) networks has been a new method to detect seismic ionospheric disturbance since 1990s [5] and it has strong imaging capability, high spatial resolution and sensibility for detecting Rayleigh wave in the ionosphere [6]. With the widely use of GPS, the properties of SID and the relationship among seismic ionospheric disturbance, earthquake and ionosphere will be better understood. By estimating the ionospheric delays of GPS [7], the total electron content (TEC) can be precisely calculated so that the seismic ionospheric anomaly signal which contain the source information related to the earthquake can be detectable from the GPS-TEC time series observation[8]. It will provide a chance to drive the complete process and the properties of the earthquake, after modeling the SID signal. On the other hand, as the short time for SID signal reach to the ionosphere (around 8 minutes), it will have potential in the near-real-time earthquake monitoring and real-time tsunami warning [9], by modeling and estimating of SID.

Hitherto, many studies for seismic ionospheric disturbance by using dense GPS measurement have been conducted. For example, Afraimovich et al. (2010) found the intensive N-shaped shock-acoustic waves with a plane waveform following the 2008 Wenchuan earthquake [10]. The ionospheric disturbance following the 2015 Mw 7.8 Nepal Earthquake is detected by GPS-TEC and it is caused by the acoustic gravity wave induced by Rayleigh wave [11]. Zhou et al. (2017) found the large-scale ionospheric anomalies near the epicenter two days prior to the same 2015 Mw 7.8 Nepal Earthquake from GPS observations of the Crustal Movement Observation Network of China (CMONOC) [12]. Another seismic ionospheric perturbation following the Mw 9.0 Tohoku Earthquake in Japan was found from nationwide GPS receiving networks and the disturbance was confirmed existing three different propagation velocities [13,14,15].

Although numerous previous studies have detected and estimated the seismic ionospheric disturbance, there are still problems and difficulties in studying seismic ionospheric disturbance. For instance, the distinct TEC anomaly can be detected by GPS measurement only for earthquakes with large magnitudes (Mw>6.8) [16], as the larger vertical crustal displacement or deformation cause significant CID. And the uneven distribution of ground-base GPS network makes the absence of ionospheric disturbance in some seismic regions. Besides, it is difficult to conclude the generation mechanism of CID in a simple theory, for the characteristics of CID, such as amplitude, propagation speed, period, azimuth angle, phase and waveform, vary with the factors of the earthquakes, for example, magnitude and focal mechanism[17,18] ; the pattern of rupture and ground deformation [10, 17]; the

77 geomagnetic field [9, 17] and geometry of GPS-sounding [19]. Consequently, abundant
78 investigations of different earthquake event are necessary.

79 **2. Data and Method**

80 *2.1. Earthquake information*

81 The 2020 M_w 7.7 earthquake (19.46°N,78.79°W) occurred in the Caribbean Sea to the
82 south of Cuba and northwest of Jamaica, with 10km in depth at 19:10:22(UTC), 28 January
83 2020, which is the result of the strike-slip faulting on the plate boundary between the North
84 America and Caribbean tectonic plates. The epicenter is located at the plate boundary and the
85 fault plane strikes along with the orientation of the plate boundary. The GPS observation data
86 with a sampling rate of 15s was obtained from dense GPS stations conducted by University
87 Navstar Consortium (UNAVCO).

88 The distribution of 93 GPS stations and 13 seismographs are shown in Figure 1 with the
89 blue triangles and red filled circles. The data of seismometers is provided by IRIS. The red
90 pentagram represents the epicenter of the 2020 M_w 7.7 earthquake and black line represents
91 the fault plane near the epicenter. The beach ball indicates the focal mechanism of the
92 earthquake event at the upper-right corner of the figure. Magnetic field (MF) parameters
93 involving inclination (I) and declination (D) are shown in the white panel at lower left quarter.
94 The slip distribution map of the 2020 M_w 7.7 Jamaica earthquake is shown in Figure 1(b).
95 Related information (finite fault and slip distribution) of this earthquake event is accessible
96 form U.S. Geological survey (USGS). The slip distribution map indicates the motion direction
97 of fault plane in strike of 258° with arrows and slip amplitude in color.

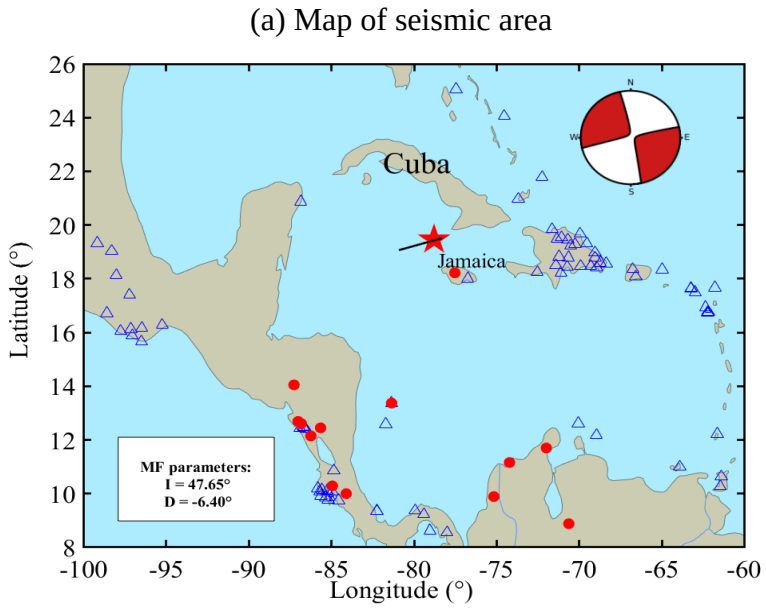

98

(b) Slip distribution map

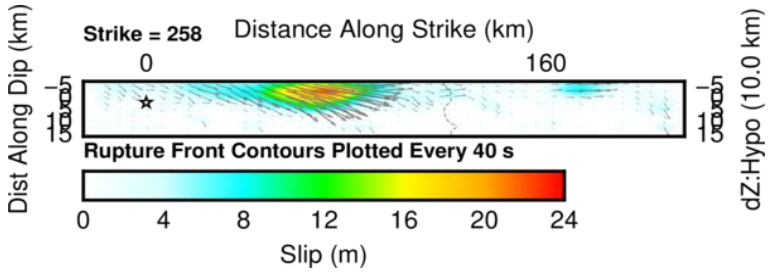

Figure 1. The Mw 7.7 Jamaica earthquake event. (a) Distribution of GPS stations and seismographs around the epicenter area and basic information about the earthquake. (b) The slip distribution map from USGS (https://earthquake.usgs.gov).

2.2. Method

The ionosphere disturbances can be extracted from GPS-TEC time series. During the propagation of GPS satellite signals, the ionosphere delay in signals relates to the GPS signal frequency and ionosphere TEC. Therefore, in order to get the ionosphere disturbances, the ionosphere TEC should be calculated precisely from the dual-frequency GPS observation (f_1 = 1,575.42 MHz, f_2 = 1,227.60 MHz) by the following equation [20,21]:

$$STEC = \frac{f_1^2 f_2^2}{40.3\left(f_1^2 - f_2^2\right)}\left(L_1 - L_2 + \lambda_1\left(N_1 + b_1\right) - \lambda_2\left(N_2 + b_2\right) + \varepsilon_L\right)$$

$$STEC = \frac{f_1^2 f_2^2}{40.3\left(f_1^2 - f_2^2\right)}\left(P_1 - P_2 - \left(d_1 - d_2\right) + \varepsilon_p\right)$$

Where STEC is slant total electron content, L_1 and L_2 are the GPS carrier phase measurements, P_1 and P_2 are the GPS code measurements, λ_1 and λ_2 are the GPS signal wavelength, N is the ambiguity, b is the instrument biases for carrier phase, d_1 and d_2 are the differential code biases, and ε is the residual. STEC represents the absolute magnitude of ionosphere TEC. In order to get the relative variation of the ionosphere TEC and estimate the characters of seismo-ionospheric disturbances, the STEC along the GPS line of sight (LOS) is required to be vertical TEC(VTEC) converted by the following mapping function:

$$VTEC = STEC * \cos\left[\arcsin\left(\frac{R\sin\left(z\right)}{R+H}\right)\right]$$

Where H is the height of the ionosphere shell, in this article, H is assumed at 350km of altitude. R is the earth's radius, and z is the elevation of the satellite. The calculated VTEC is used in forming GPS-TEC time series. However, cycle slip is the main error in obtaining high-precision TEC values from above method [22]. Therefore, the second-order time-difference phase ionospheric residual (STPIR) was used to eliminate cycle slip in this article [23]. Besides, the background noise of ionosphere and TEC variation should be taken into consideration in order to get the precise GPS-TEC time series. In this article, the

Butterworth filter of a fourth-order zero-phase finite impulse was used to remove the background noise and obtain the filtered TEC series, which related to the earthquake. According to the Nyquist sampling theory, the Nyquist frequency is about 8mHz for GPS observation which sampling interval is 60s. In this article, the sampling interval of GPS observation data is 15s, thus the Nyquist frequency is larger than 8mHz. As 2mHz is the cutoff frequency of acoustic above the ionospheric height. The GPS-TEC time series obtained from station LMNL and satellite PRN26 with different passband frequency are shown in Figure 2. As shown in Figure 2, the distinct seismo-ionospheric disturbance can be found out from the series with the 2-5mHz passband frequency about 12 min after the occurrence of the earthquake in the red lines marked zone, so the fourth-order zero-phase Butterworth filter with passband frequency of 2 and 5mHz was used to obtain the GPS-TEC time series.

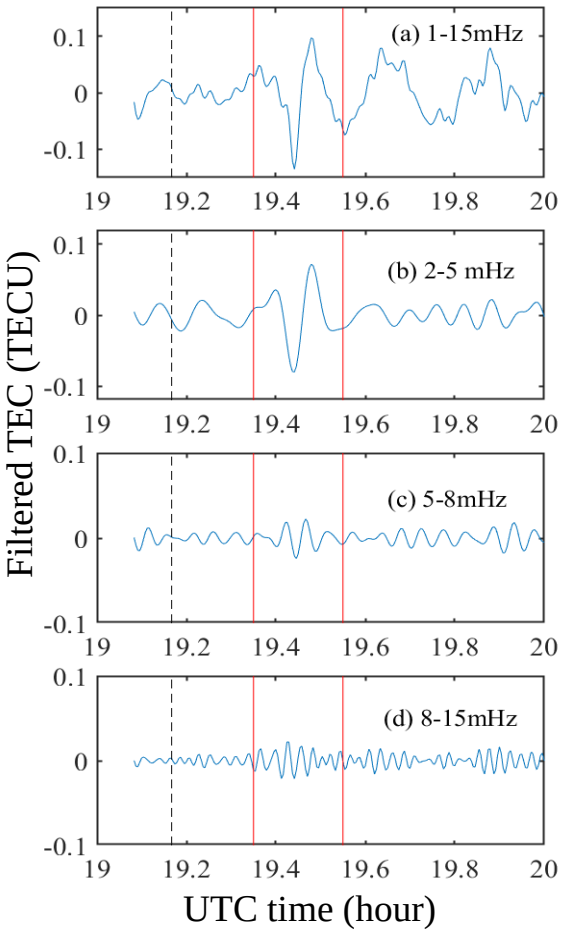

Figure 2. GPS-TEC time series observed by station LMNL and satellite PRN26with different filter passband frequency. (a) TEC series with 1-15mHz passband. (b) TEC series with 2-5mHz passband. (c) TEC series with 5-8mHz passband (d) TEC series with 8-15mHz passband. The dashed black line represents the eruption time of the 2020 Jamaica earthquake.

3. Results and discussion

3.1. Co-seismic ionospheric disturbances

By using the GPS measurement, the TEC responses and co-seismic ionospheric disturbances following the 2020 Jamaica earthquake are detected and estimated. Figure 3 shows the TEC distribution maps from 19:10 UTC to 19:30 UTC. The red pentagram represents the epicenter and the colorful filled dot is corresponding to the subionospheric point (SIP) and the positions of these dots represent the locations of SIPs. The color values show the variation amplitude of filtered TEC and the color bar indicates the variational value range of filtered TEC series (in TECU). As is shown Figure 3, the 2020 Jamaica earthquake occurred at 19:10 UTC. However, there are no obvious ionospheric anomalies at first (Figure 3a). After about 12 min of the main shock, significant ionospheric anomalies are first detected at the southeast region of epicenter (200-450km away from the epicenter). Most of the TEC disturbances display in positive anomalies (Figure 3b). The average variation amplitude of these TEC disturbances reaches to 0.05 TECU (1 TECU = 10^{16} e/m^2). Around 3min later at 19:25 UTC, the TEC disturbances become stronger and the variation amplitude reaches its maximum which is about 0.07TECU at this time. It should be noticed that the TEC disturbances turn positive anomalies to negative anomalies (Figure 3c). The negative TEC anomalies last for around 3min and turn back to positive anomalies in the same area at 19:28 UTC (Figure 3d). The amplitude of TEC disturbances begins to deplete, which is about 0.04TECU. Besides, another significant ionospheric anomaly is detected at the southwest area around 700-800km away from the epicenter at 19:26 TECU (Figure 3e).. The TEC disturbances have a larger variation amplitude which reaches to 0.07 TECU. After the same time interval as the previous discussed TEC disturbance (3 min), the TEC disturbances show an opposite polarity change (Figure 3f) at 19:29UTC. After 19:30 UTC, no obvious TEC disturbances can be detected. Based on above preliminary estimate, two TEC disturbances exist in different azimuth of the seismic region.

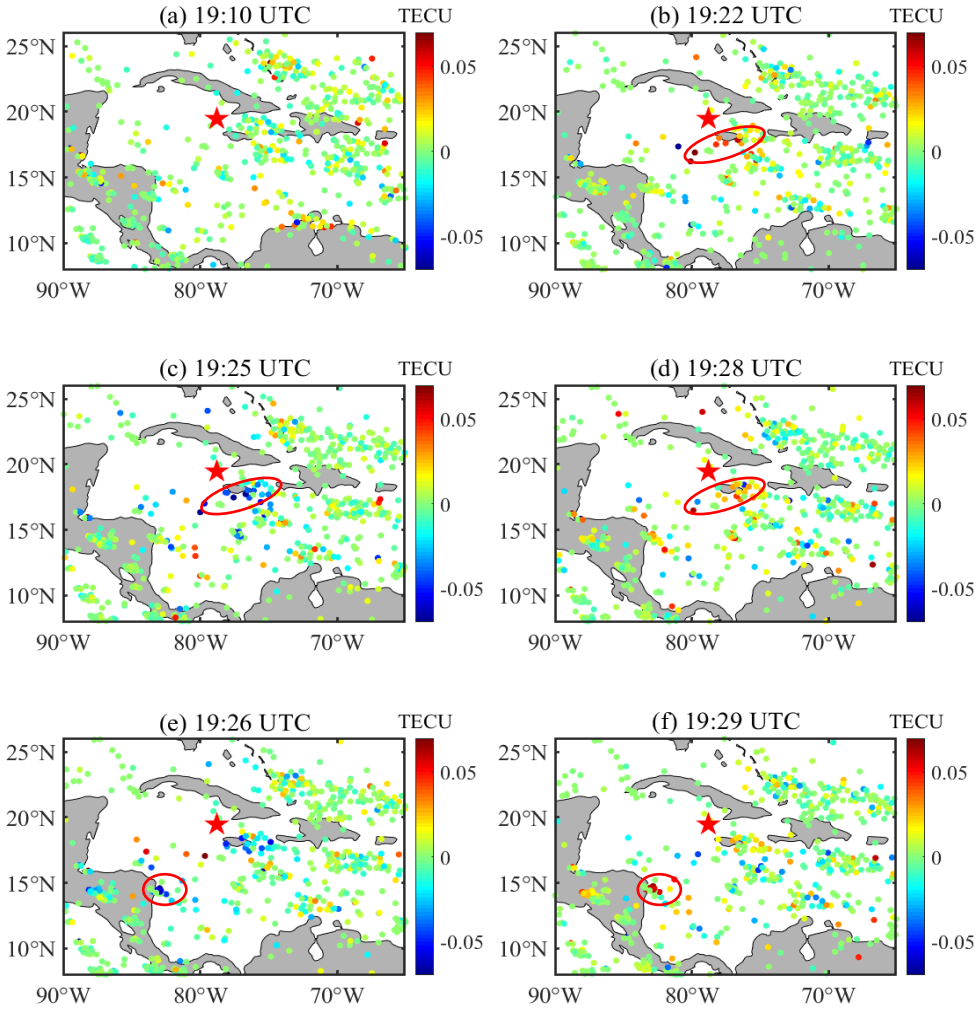

167

168 **Figure 3.** Filtered TEC distribution maps during 19:10-19:30 UTC. The red pentagram
169 represents the location of the epicenter and the color filled dots indicate the positions of SIPs.
170 The color bar is the variational value range of filtered TEC.

171 In order to comprehend the relationship between earthquake and seismic ionospheric
172 disturbance, the further specific characteristics of the TEC disturbances should be estimated.
173 Figure 4 shows the SIP tracks between the satellites and the stations at the height of 350km
174 during 18:45-20:00 UTC. It can be seen that the SIP tracks obtained from the two satellites
175 cover the most area around south of the epicenter. The SIP tracks of PRN03 mainly cover the
176 southeast area of the epicenter while the PRN26's mainly cover the northwest, southwest and
177 northeast area.

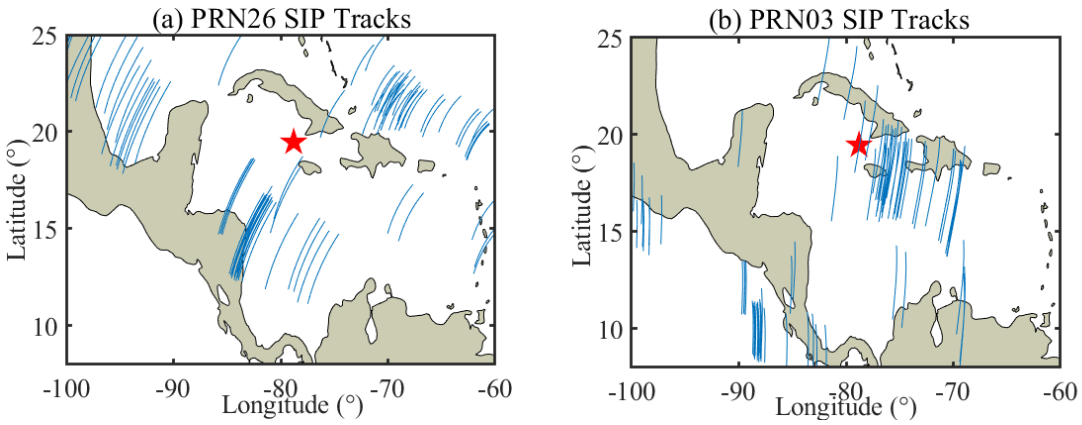

Figure 4. The SIP tracks between the satellites and the stations. (a) The SIP tracks with PRN26. (b) The SIP tracks with PRN03.

Figure 5 shows more detailed characters about these two TEC disturbances. It shows the SIP tracks of station CN35 with PRN26 (Figure 5a) and station JME2 with PRN03 (Figure 5b) during 19:05-20:00 UTC, corresponding filtered GPS-TEC time series and the changes in the satellite elevation angle and distance. The two graphs on the left displays the SIP tracks, the red pentagram represents the location of epicenter, the blue triangles represent the location of station CN35 and JME2. Both SIP tracks locate in the near-field of the epicenter. The middle two displays the GPS-TEC time series in typical N-shaped waveform observed by station CN35 with PRN26 and station JME2 with PRN03. The dashed line indicates the eruption time of the 2020 Jamacia earthquake. The distinct ionosphere disturbance can be observed clearly after about 12min of the main shock from both series. The difference is that the negative variation amplitude of the series observed by station CN35 with PRN26 reaches more than 0.15 TECU, while the negative variation amplitude of station JME2 with PRN03 reaches only to 0.07 TECU. The changes in the satellite elevation angle (in blue line) and distance (in orange line) are shown in the right two graphs. The satellite elevation angle between station CN35 and satellite PRN26 decreases from 40° to 22°, while the satellite elevation angle between station JME2 and satellite PRN03 decreases from 31° to 25°. These two elevation angles both belong to low elevation angle range, which is sensitive to the detection of co-seismic ionospheric disturbances caused by big earthquakes [24].

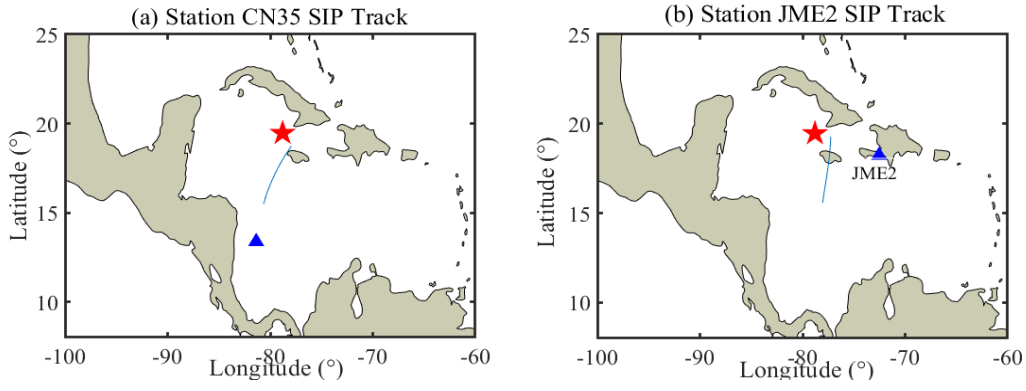

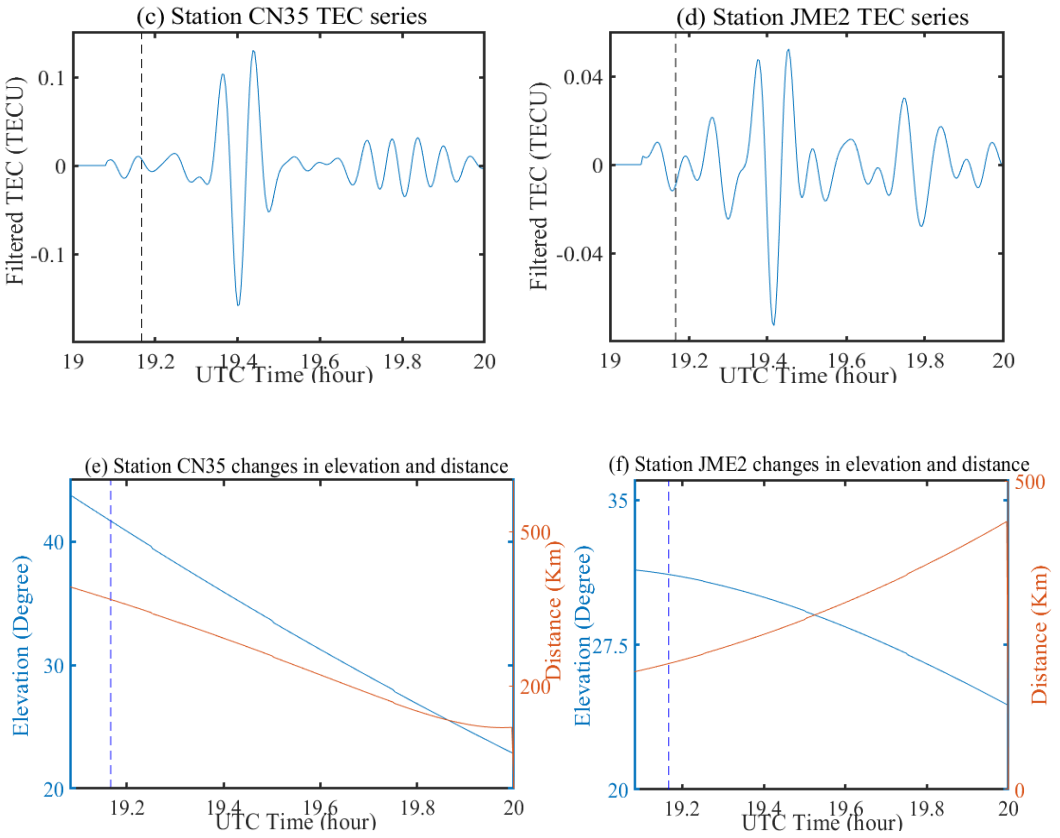

Figure 5. (a) SIP track observed by station CN35 with satellite PRN26. (b) SIP track observed by station JME2 with satellite PRN03. (c) TEC series from station CN35, PRN26 observation. (d) TEC series from station JME2, PRN03 observation. (e) Changes in elevation and distance of station CN35,PRN26. (f) Changes in elevation and distance of station JME2,PRN03.

3.2. Two-azimuth disturbances

The earthquakes may excite a variety of different co-seismic ionospheric disturbances. For example, the two-mode ionospheric disturbances are detected and estimated following the 2005 Northern California offshore earthquake [24]. And Astafyeva et al. (2009) found another two-mode long-distance co-seismic ionospheric disturbance following the great 1994 Kurile earthquake [25]. The research for propagation characters of ionospheric disturbances can demonstrate the pattern, modes, generation mechanism and source of co-seismic ionospheric disturbances. In section 3.1, we have found two ionospheric disturbances in different azimuth. In this section, the generation source and further characteristics of the two disturbances are estimated and discussed. Figure 6 shows the traveling-time diagrams of filtered GPS-TEC time series from satellites PRN26 and PRN03. These two diagrams demonstrate the linear relationships between the seismic ionospheric disturbance travel time and distance from SIP to the epicenter. The color of the curves indicates the variation value of filtered TEC series. Two significant ionospheric disturbances can be found through the traveling-time diagrams. After performing the linear fit, the propagation velocity of the ionospheric disturbances detected by PRN26 is about 2.53km/s while the PRN03's is around 2.57km/s.

The ionospheric disturbance generated by different sources can be distinguished through the velocity of their propagation. These two velocities are larger than sound speed at the ionospheric altitude(~1km/s) but lower than the Rayleigh surface wave propagation speed which propagates along the ground surface with velocity 3000-4000m/s [26]. According to Jin (2018), the two ionospheric disturbances are probably both the secondary acoustic wave generated by seismic Rayleigh waves with dynamic coupling [24].

In the left diagram, the disturbance is detected by PRN26 after 12 min of the main shock in 300- 800km away from the epicenter. The amplitude of the negative polarity is larger than 0.08 TECU. On the other hand, the disturbance detected by PRN03 at the same time in 250-500km away from the epicenter has a lower negative amplitude which only reaches to 0.05 TECU. Therefore, the two disturbances have different amplitude characteristics.

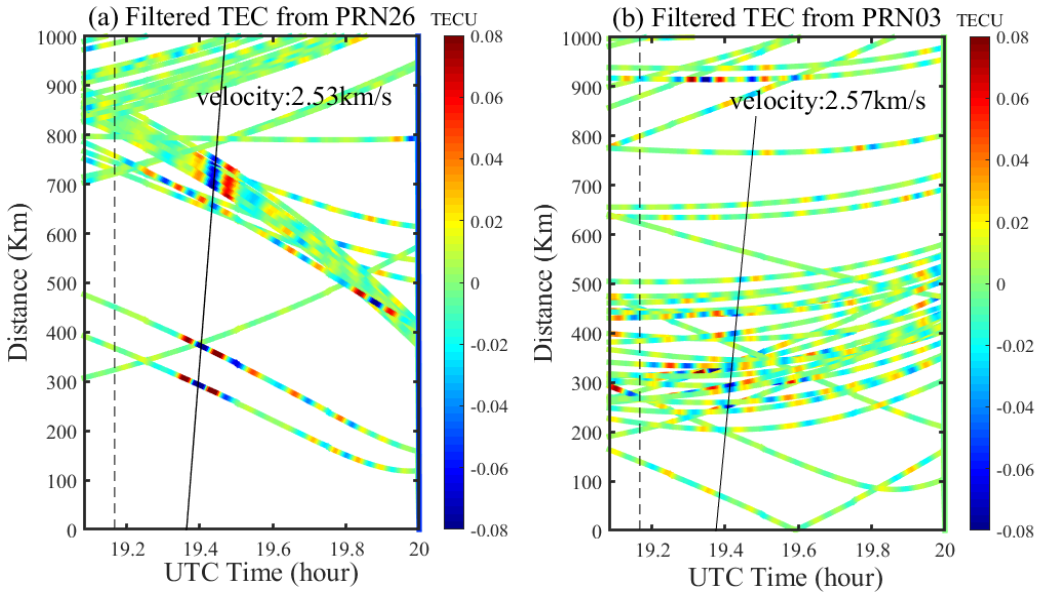

Figure 6. Traveling-time diagrams of seismic ionospheric disturbances from PRN26 (a) and PRN03 (b). The dashed black line represents the eruption time of the 2020 Jamaica earthquake. The color bars indicate the value range of filtered TEC series. The black diagonal line is used to linear fit the propagation velocity of TEC disturbances.

Figure 7 shows the distribution of IPP epicentral azimuth and elevation angle of the maximum in each GPS-TEC time series. The color of dot indicates the value of the maximum. As is shown in the left scatter diagram (Figure 7a), the dots which larger than 0.03 TECU are mainly at the elevation angles 12-30° of corresponding line of sight (LOS). The dots are mainly at elevation angles 15-30° of corresponding LOS in the right scatter diagram (Figure 7b). The distribution of the GPS elevation angle contributes to distinguish the horizontal and vertical disturbance acoustic wave propagations. The elevation angles corresponding to the maximum in each GPS-TEC time series with PRN26 and PRN03 are both in the range of low elevation angles. Therefore, the two ionospheric disturbances both propagate along vertical direction to the ionosphere.

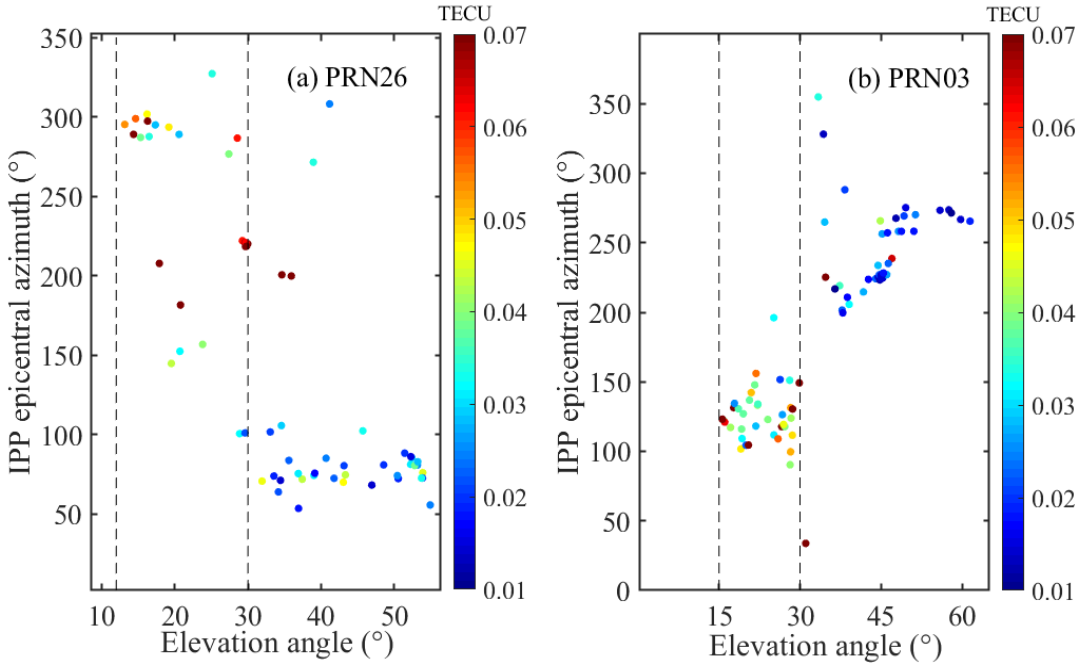

Figure 7. (a) Distribution of IPP epicentral azimuth and elevation angle of the maximum in filtered TEC series observed from PRN26. (b) Distribution of IPP epicentral azimuth and elevation angle of the maximum in filtered TEC series observed from PRN03. The maximum filtered TEC less than 0.01 TECU are neglected.

Figure 8 shows the change curves in the elevation angles and SIP epicenter azimuth of the stations which have detected the ionospheric disturbances in the form of polar diagram from 19:00-20:00 UTC. The theta axis represents the SIP epicentral azimuth (in degree). The radius axis represents the elevation angles (in degree). The red pentagram represents the corresponding elevation angle and epicenter azimuth at the eruption time of the earthquake. It can be clearly seen from the curves that all the elevation angles are low angles and the values of angle are decreasing since the eruption time of earthquake. According to previous work [26], lower elevation angle can enlarge the horizontal extent of the ionospheric region. When the disturbance wave vector is perpendicular to satellite-to-receiver line of sight (LOS), the observed amplitude reaches to largest amount. On the other hand, the amplitude of the disturbance signal is relevant to the satellite elevation angle. However, with the combination of Figure 7 and Figure 8, the elevation angles of the IPP or SIP observed by PRN03 and PRN26 are both at the low angle range. Besides, the consistent trend in the change of elevation angle can be clearly found. Thus, ionospheric disturbance can be detected more easily at low satellite elevation angle.

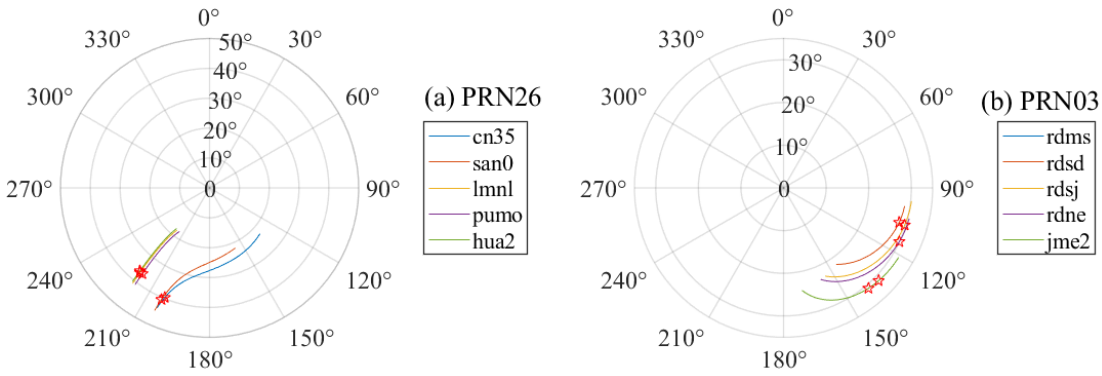

Figure 8. The polar diagram of the changes in the elevation angles and SIP epicenter azimuth of selected stations with satellite PRN26(a) and PRN03(b) during 19:00-20:00 UTC.

Figure 9(a) shows the distribution of the SIP epicenter azimuth for the maximum of each GPS-TEC time series in the form of polar diagram. The theta axis represents the SIP epicenter azimuth (in degree). The radius axis represents the variation value of the filtered TEC (in TECU). The north direction is set as the 0° azimuth. The red hollow dot represents the maximum of TEC series obtained from PRN03 and the blue hollow dot represent the maximum of TEC series observed by PRN26. The maximums of TEC series detected by PRN26 which are larger than 0.05 TECU mainly locate around epicenter azimuth 210°, while the maximums of TEC series obtained from PRN03 which are larger than 0.05 TECU mainly locate at epicenter azimuth 120-150°. This confirms that two different ionospheric disturbances exist in southwest and southeast area respectively combined with the result of TEC distribution maps in Figure 3(c) and (e). Figure 9(b) is Rayleigh waves radiation pattern at 0.01Hz frequency graph. The theta axis represents the azimuth (in degree) and the radius axis represents the amplitude of Rayleigh waves at 0.01Hz (in m/Hz). Relevant azimuth and amplitude data is downloaded from IRIS. Radiation pattern graph describe the amplitude component of Rayleigh waves in all directions. The amplitude of Rayleigh waves at 0.01 Hz reaches peak value in direction of azimuth 120° and 210°, which is consistent with the azimuth distribution of the two ionospheric disturbances. It indicates that the Rayleigh waves propagating along southwest direction (around azimuth 210°) and southeast direction (around azimuth 120°) have a large vertical displacement amplitude to induce the co-seismic ionospheric disturbance.

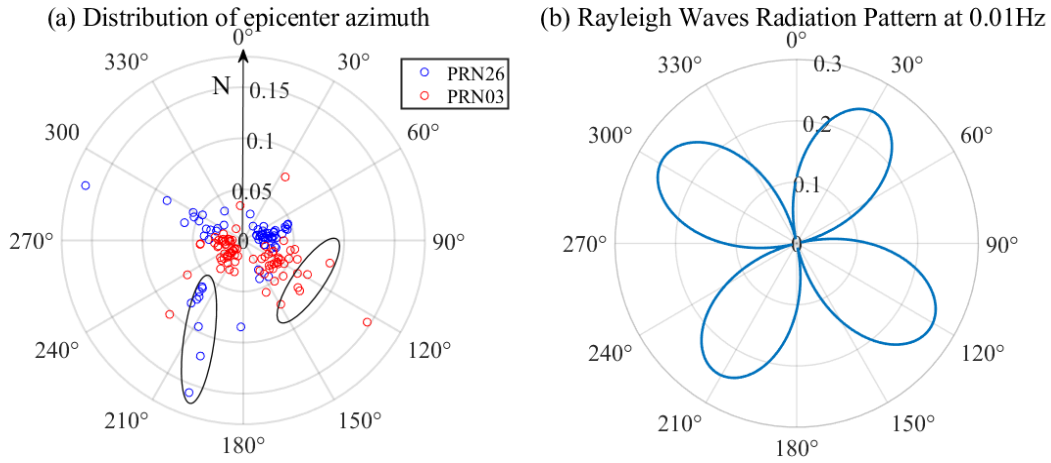

Figure 9. (a) The polar diagram of the distribution of the SIP epicenter azimuth for the maximum of each GPS-TEC time series. (b) Rayleigh waves radiation pattern diagram at 0.01Hz frequency.

Figure 10 shows the distance distribution of the maximum in each TEC series for the ionospheric disturbances detected by satellite PRN26 and PRN03. The red triangles represent the maximum amplitude of TEC series observed by PRN26 and the blue circles represent the TEC series observed by PRN03. The TEC series obtained by PRN03 have the maximum amplitude lower than 0.06 TECU in the range of 200-450km away from the epicenter, while PRN26 detect larger amplitude TEC disturbances which are larger than 0.06 TECU in 300-800km away from the epicenter. Therefore, combined with the TEC distribution maps shown in Figure 3, the two disturbances detected by PRN26 and PRN03 respectively differ in amplitude and distance distribution characteristic.

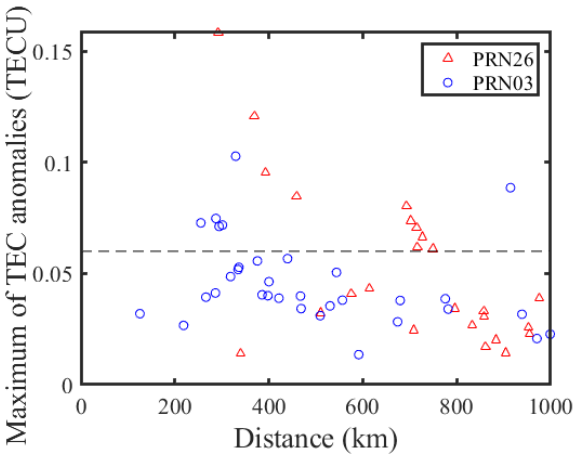

Figure 10. distance distribution of the maximum of each TEC series for the ionospheric disturbances detected by satellite PRN26 and PRN03. The red triangles represent the TEC series observed by PRN26 and the blue circles represent the TEC series observed by PRN03.

3.3. CID waveform and spectrum signature

Analysis for disturbances signal waveform and spectrum can provide more information about characteristics of the two-azimuth ionospheric disturbances to distinguish their differences . Figure 11 shows some cases of disturbances signal waveforms and seismic waveforms in southwest and southeast direction. Disturbance waveforms observed by PRN26 are shown in Figure 11(a), while disturbance waveform observed by PRN03 are displayed in Figure 11(c). The x-axis represents the UTC time. The dashed black line represents the eruption time of the earthquake, the name of selected station is located in the right side of each corresponding waveform. The significant TEC disturbances can be distinguished from the waveforms after about 12 min of the main shock, which is in consistent with the results of TEC distribution map shown in Figure 3 and traveling-time diagrams of seismic ionospheric disturbances shown in Figure 6. As the distance between selected station and epicenter increases, the amplitude of waveforms become to decrease, and the appearance time of ionospheric disturbances begin to delay. It is noticeable that, in Figure 11(a), the signals observed by station CN35 and SAN0 show a typical N-shape waveform. However, as the

distance from epicenter increases, the waveforms observed by far-field station LMNL, PUMO, LEPA, PUJE, HUA2 and GRZA appear in the form of an inverted N-shaped waveform (negative half-phase appear first [27]). In Figure 11(c), all the waveforms have N type forms, which is different from the waveforms of selected stations with PRN26. The detection of inverted N-shape and N-shape waveform indicates polarity divergence in the two-azimuth ionospheric disturbances. With the same passband filtering, the seismic wavesforms at 2-5mHz in southwest and southeast direction from the vertical broadband high-gain seismometers are shown in Figure 11(b) and (d) respectively. The y-axis represents the distance between seismograph and epicenter. And the x-axis indicates UTC time. Through liner fitting, the group speed of seismic waves in southwest direction is about 3.75km/s, which is close to the speed 3.76km/s in southeast direction. These two propagation speed are both in the velocity range of Rayleigh surface wave. Besides, it should be noticed that the seismic waves in SW show a negative polarity, which is consistent with the inverted N-shape waveform of Rayleigh wave-induced ionospheric disturbance observed by PRN26 in the southwest area. The same result can be concluded by comparing Figure 11(c) and (d). It is believed that the polarity of co-seismic ionospheric disturbance is determined by the polarity of generation source wave.

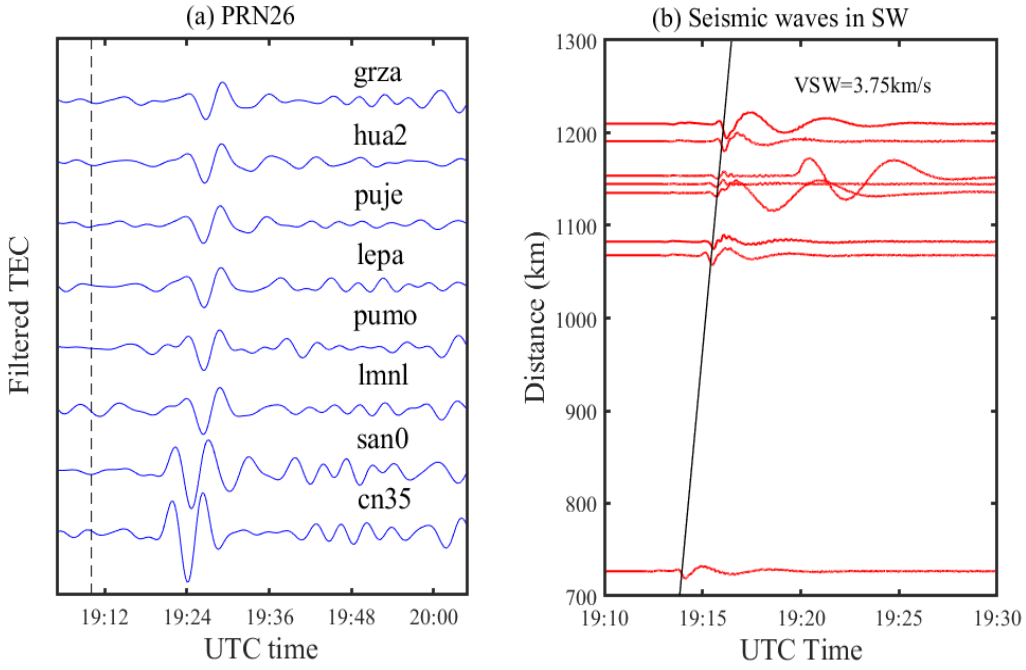

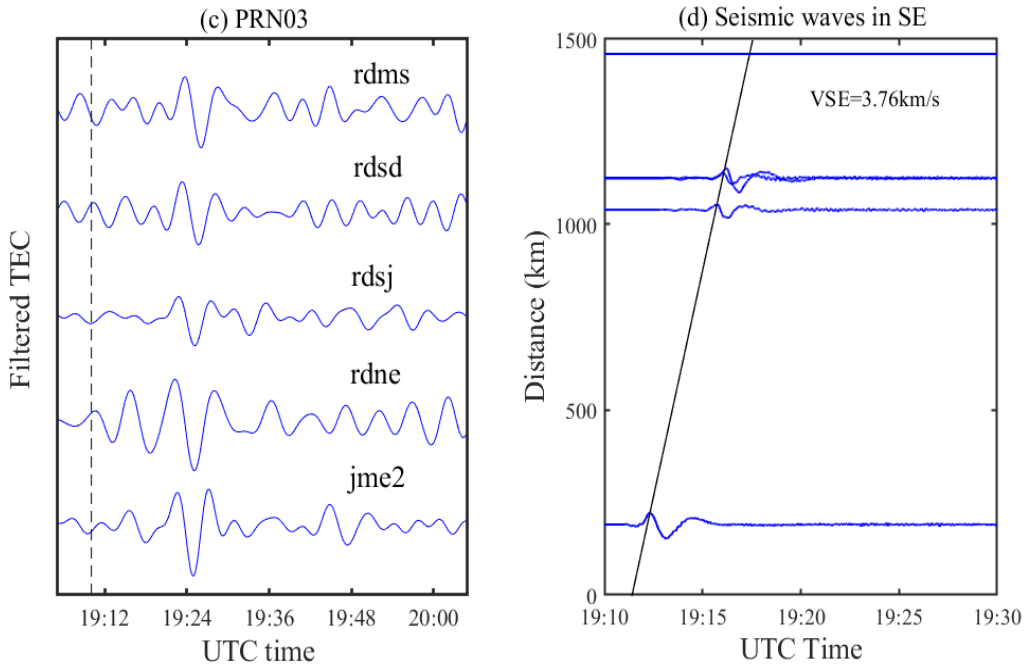

344

345

346 **Figure 11.** (a) Disturbance waveforms from observation of selected stations in PRN26. (b)
347 Seismic waves in southwest direction (c). disturbance waveforms from observation of selected
348 stations in PRN03. (d) Seismic waves in southeast direction.

349 Furthermore, Figure 12 shows the spectrograms of TEC disturbances series from selected
350 stations and satellites after using short-time Fourier transform (STFT) to convert TEC series
351 from time domain to the frequency domain. The diagram order is station CN35 for PRN26,
352 station HUA2 for PRN26, station JME2 for PRN03 and station RDMS for PRN03 respectively.
353 The left panel displays the TEC time series in blue line and distance changes in orange line,
354 and the right panel represents the spectrogram of corresponding TEC time series converting
355 from STFT. The center frequency of disturbance signals for station CN35 and station GRZA is
356 about 3.4mHz and 3mHz, while frequency of disturbance signals for station JME2 and station
357 RDMS is centered at about 3.3mHz and 3.1mHz. The center frequencies for selected stations
358 are all in the frequency range of infrasonic wave. Therefore, the two ionospheric disturbances
359 detected by PRN26 and PRN03 show a same frequency characteristic..

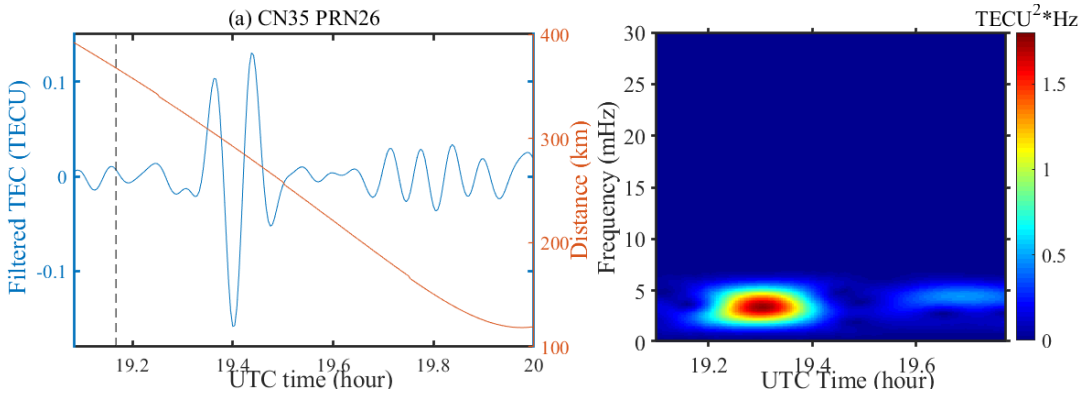

360

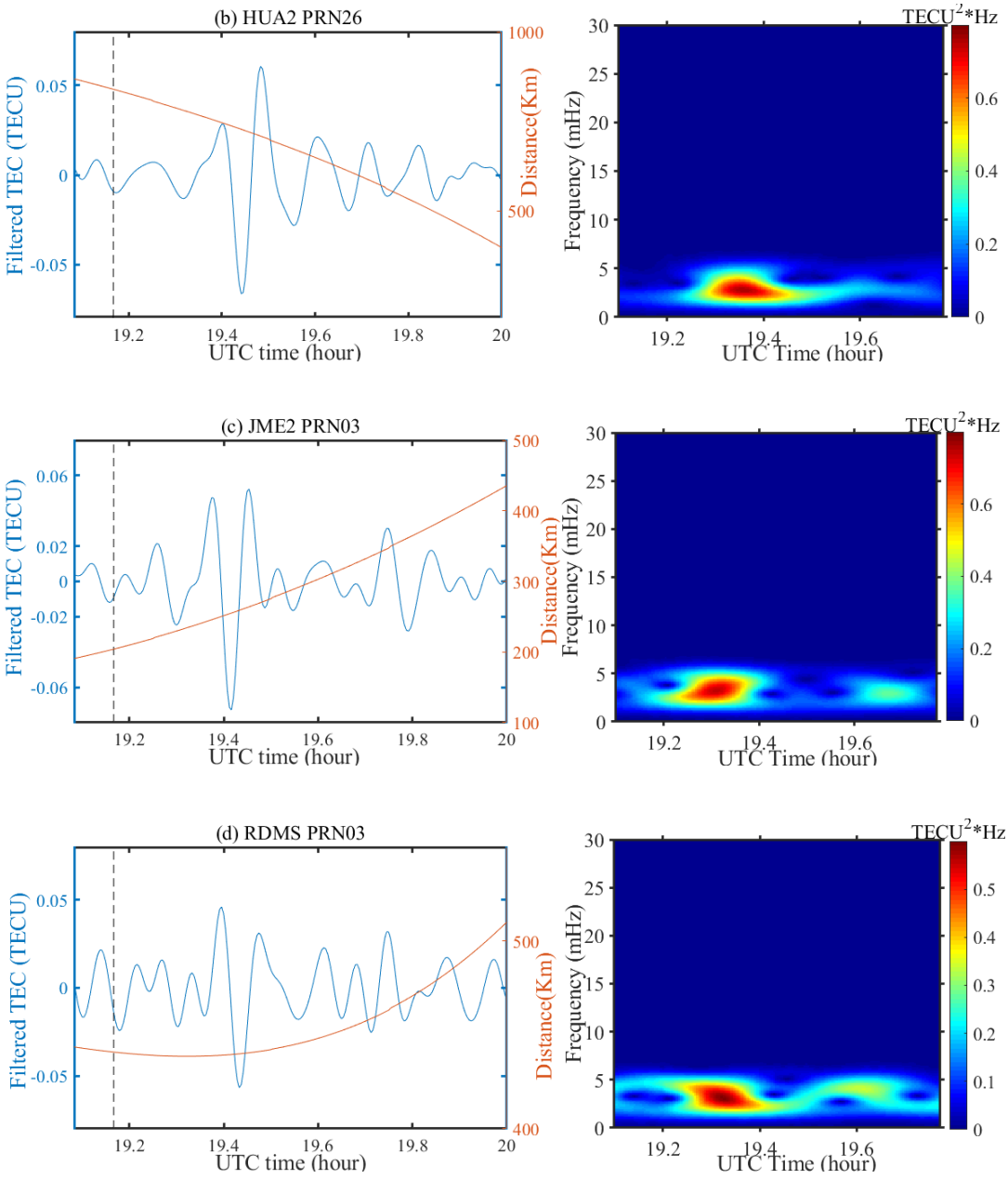

Figure 12. The spectrograms of TEC disturbances series from selected stations and satellites. (a) Station CN35 of satellite PRN26. (b) Station GRZA of satellite PRN26. (c) Station JME2 of satellite PRN03. (d) Station RDMS of satellite PRN03.

3.4. Discussion

The eruption of the 2020 Jamaica strike-slip earthquake excites seismic Rayleigh surface waves which propagate along the southwest direction (around azimuth 210°) and southeast direction (around azimuth 120°). The Rayleigh surface waves induce the secondary acoustic wave with dynamic coupling in a few kilometers away from epicenter and cause TEC fluctuation in the ionosphere height, and the distinct co-seismic ionospheric disturbances, appear and are detected by GPS observation after about 12min of the main shock. The

detection of distinct TEC disturbance demonstrate that the strike-slip Jamaica earthquake can also cause large amount vertical displacement [26,28], although the amount is still less than a dip-slip earthquake of the same magnitude. The maximum variation amplitude of TEC series obtained from GPS measurement reaches more than 0.1 TECU. The amplitude of TEC series decreases with the increasing distance between SIPs and epicenter. The TEC disturbances appear in the southeast near-field and southwest far-field area of the epicenter and last for less than half an hour, when combined with the TEC distribution maps in Figure 3. Satellite PRN26 and PRN03 detected two different TEC disturbances respectively during the 2020 Jamaica earthquake. Furthermore, the propagation velocity, amplitude, frequency, maximum of TEC series and corresponding elevation angle and azimuth changes from the two-azimuth TEC disturbances are estimated and analyzed in above sections. We have discussed the CID source through estimating the propagation speed and frequency characteristic of the disturbance signals. Besides, the azimuthal asymmetry of CID amplitude and the detection of the inverted *N*-shape waveform in seismic ionospheric disturbance are the main differences and may reveal the deep relationship among CID, Rayleigh wave and earthquake..

As is mentioned in section 3.3, the disturbance signals display in the forms of inverted N-shape wave and typical N-shape wave. This demonstrates that the two-azimuth ionospheric disturbances appear in different initial polarity attribute to different ground-motion pattern. Astafyeva and Heki (2009) suggested that the waveform of disturbance signals repeat the initial ground crustal motion. The typical and inverse N-shape wave are caused by mixed type of focal mechanism [17]. Besides, according to Kiratzi (2014), the focal mechanism can be determined by the first motion polarity of the body and surface wave [29]. Figure 13 represents the schematic diagram for focal mechanism. The P-axis, T-axis, fault plane and auxiliary plane are labeled in the diagram.The origin represents the hypocenter and the theta axis shows the epicenter azimuth (in degree). It indicates that during the slip, the southwest quadrant is a compression region while the southeast quadrant can be considered as a dilatation or extension region. Thus, the appearance of inverted N-shaped wave in the southwest area detected by PRN26 attributes to the negative co-seismic vertical crustal movement, and the typical N-shape wave detected in the near-field southeast area ascribes to the co-seismic vertical ground uplift. This conclusion matches the Rayleigh waves shown in Figure 11(b) and (d).

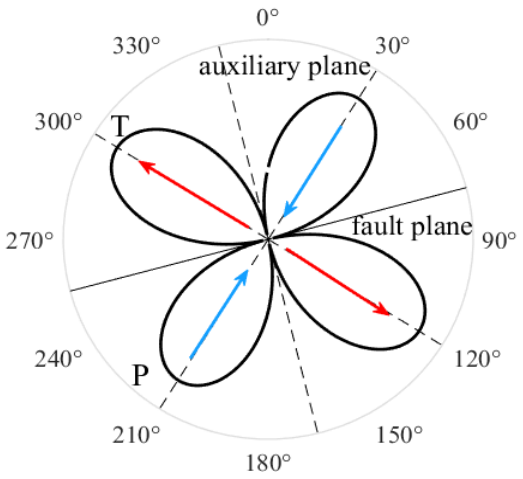

Figure 13. Schematic diagram for focal mechanism.

However, Rolland et al (2013) argued that the amplitude and waveform of TEC signals may be controlled by other factors, such as geomagnetic filed, geometry of GPS-sound and background ionization. Thus, we obtained the detailed information about the geomagnetic field near the epicenter area using the IGRF model from National Oceanic and Atmospheric Administration (NOAA, https://www.ngdc.noaa.gov). The geomagnetic field has a westerly declination around 6.40°, and an inclination 47.65° at the ionosphere height of 350km. It can be concluded that the geomagnetic filed hardly influence the amplitude and phase of CID, as the Rayleigh-induced disturbance wave vector in two azimuths propagate at small angles (less than 30°) to the MF line [9, 26]. Besides, no distinct TEC anomaly can be detected on the north from the epicenter, which is consistent with the 'ionospheric radiation pattern' derived from Rolland et al (2013).

As for the azimuthal asymmetry of CID amplitude, however, we have discussed the factor of GPS-sounding geometry and suggested that the elevation angle is not the main reason for azimuthal asymmetry of CID amplitude in section 3.2. We infer that the azimuthal asymmetry of CID amplitude may attribute to the factors of vertical and horizontal crustal displacements in different azimuths, even, the propagation media for CIDs. However, as the absence of the TEC-time series for PRN26 during the range of 400-700km away from the epicenter, further researches about the influence of horizontal and vertical crustal displacement in the amplitude of CIDs are needed in the future.

4. Summary

In this article, the ionospheric responses following the 2020 M_w 7.7 Jamaica earthquake are studied and estimated by dense GPS measurements. The co-seismic ionospheric disturbances are significantly detected by Satellite PRN26 and PRN03 in two different azimuths after about 12min of the main shock. The one exists in the southwest area 800km away from the epicenter with the propagation velocity of 2.53km/s, while the other is detected by PRN03 in the southeast area 200-450km away from the epicenter with the speed of 2.57km/s. The variation amplitude of the disturbances detected by PRN26 is larger than the PRN03's. The average variation amplitude of the disturbances detected by PRN26 reaches to 0.08 TECU, while the PRN03's reaches only to 0.05TECU. Besides, the center frequency of the selected disturbances signals detected by PRN26 are about 3.4mHz and 3mHz, while the disturbances signals detected by PRN03 are centered at 3.3mHz and 3.1mHz. These disturbance signals all belong to infrasonic wave. Finally, by estimating the characteristic of CID, the two-azimuth ionospheric disturbances are both secondary acoustic waves in the infrasonic frequency range induced by the seismic Rayleigh surface wave propagating along southwest direction and southeast direction with dynamic coupling.

Acknowledge:

This work was supported by the National Natural Science Foundation of China (NSFC) Project (Grant No. 12073012) and National Natural Science Foundation of China-German

Science Foundation (NSFC-DFG) Project (Grant No. 41761134092). Great gratitude to UNAVCO for providing the GPS observation data, IRIS seismograph data and Rayleigh wave radiation pattern data (http://www.iris.edu) and NOAA (http://www.ngdc.noaa.gov) for providing geomagnetic filed information.

References

1. Ronald V. Row. Evidence of Long-Period Acoustic-Gravity Waves Launched into the F Region by the Alaskan. *Journal of Geophysical Research,* **1966**, 71(1):343-345.

2. Ronald V. Row. Acoustic - gravity waves in the upper atmosphere due to a nuclear detonation and an earthquake. *Journal of Geophysical Research,* **1967**, 72(5):1599-1610.

3. R. S. Leonard, R. A. Barnes, JR. Observation of Ionospheric Disturbances Following the Alaska Earthquake. *Journal of Geophysical Research,* **1965,** 70(5):1250-1253.

4. Davies K, Baker D M. Ionospheric effects observed around the time of the Alaskan earthquake of March 28, 1964. *Journal of Geophysical Research*, **1965**, *70*(9):2251-2253.

5. Calais, E., Minster, J. B. GPS detection of ionospheric perturbations following the January 17, 1994, Northridge earthquake. *Geophysical Research Letters,* **1995,** 22(9):1045-1048.

6. Giovanni Occhipinti, Philippe Dorey, Thomas Farges, et al. Nostradamus: The radar that wanted to be a seismometer. *Geophysical Research Letters,* **2010,** 37(18).

7. Jin, S. G., Wang, J., Zhang, H., and Zhu, W. Y. Real-time monitoring and prediction of the total ionospheric electron content by means of GPS observations. *Chinese Astronomy and Astrophysics,* **2004**, 28(3):331 – 337.

8. Jin, S. G., Jin, R., Kutoglu, H. Positive and negative ionospheric responses to the March 2015 geomagnetic storm from BDS observations. *Journal of Geodesy,* **2017,** 91(6):613-626.

9. Rolland, L. M., Vergnolle, M., Nocquet, J. M., et al. Discriminating the tectonic and non-tectonic

contributions in the ionospheric signature of the 2011, Mw 7.1, dip-slip van earthquake, eastern Turkey. *Geophysical Research Letters,* **2013,** 40:2518-2522.

10. Afraimovich E L, Ding F, Kiryushkin V V, et al. TEC response to the 2008 Wenchuan Earthquake in comparison with other strong earthquakes. International Journal of Remote Sensing, **2010**, 31(13):3601-3613.

11. S. Sripathi, Ram Singh, Prabhakar Tiwari, et al. On the Co-Seismic Ionospheric Disturbances (CIDs) in the Rapid Run Ionosonde Observations Over Allahabad Following Mw 7.8 Nepal Earthquake on April 25, 2015. *Journal of Geophysical Research,* **2020,** 125(1):2169-2185.

12. Y. Zhou, et al., Ionospheric disturbances associated with the 2015 M7.8 Nepal earthquake, Geodesy and Geodynamics (2017), http://dx.doi.org/10.1016/j.geog.2017.04.004

13. Jann-Yenq Liu, Chia-Hung Chen, Chien-Hung Lin, et al. Ionospheric disturbances triggered by the

11 March 2011 M 9.0 Tohoku earthquake. *Journal of Geophysical Research,* **2011,** 116(A6).

14. Saito, A., Tsugawa, T., Otsuka, Y., et al. Acoustic resonance and plasma depletion detected by

GPS total electron content observation after the 2011 off the Pacific coast of Tohoku earthquake. *Earth, Planets and Space,* **2011,** 63(7):863-867.

15. Tsugawa T, Saito A, Otsuka Y, et al. Ionospheric disturbances detected by GPS total electron content observation after the 2011 Tohoku earthquake. AGU Fall Meeting Abstracts, **2011**.

16. Perevalova, N.P., V.A. Sankov, E.I. Astafyeva, A.S. Zhupityaeva. Threshold magnitude for ionospheric response to earthquakes, *J. Atmos. Solar-Terr. Physics,* **2014,** 108:77-90.

17. Astafyeva, E., Heki, K. Dependence of waveform of near-field coseismic ionospheric disturbances on focal mechanisms. *Earth, Planets and Space,* **2009,** 61(7):939-943.

18. K. Heki, Y. Otsuka, N. Choosakul, N. Hemmakorn, T. Komolmis, T. Maruyama. Detection of ruptures of Andaman fault segments in the 2004 Great Sumatra Earthquake with coseismic ionospheric disturbances, *J. Geophys. Res.,* **2006,** 111.

19. E.L. Afraimovich, K.S. Palamartchouk, N.P. Perevalova. GPS radio interferometry of traveling ionospheric disturbances. *J. Atmos. Sol.-Terr. Phys.,* **1998,** 60(12):1205-1233.

20. Brunini, C., Azpilicueta, F. J. Accuracy assessment of the GPS-based slant total electron content. *Journal of Geodesy*, **2009,** 83(8):773–785.

21. Jin, S.G., Jin, R., Li, D. GPS detection of ionospheric Rayleigh wave and its source following the 2012 Haida Gwaii earthquake. *Journal of Geophysical Research,* **2017,** 122(1):1360-1372.

22. Nguyen, V.K., Rovira-Garcia, A., Juan, J.M. et al. Measuring phase scintillation at different frequencies with conventional GNSS receivers operating at 1 Hz. *Journal of Geodesy,* **2019,** 93:1985-2001.

23. Cai, C., Liu, Z., Xia, P., et al. Cycle slip detection and repair for undifferenced GPS observations under high ionospheric activity. *GPS Solutions.* **2013,** 17:247-260.

24. Jin, S.G. Two-mode ionospheric disturbances following the 2005 Northern California offshore earthquake from GPS measurements. *Journal of Geophysical Research,* **2018,** 123:8587-8598.

25. Astafyeva, E., Heki, K., Kiryushkin, V., Afraimovich, E., and Shalimov, S. Two‐mode long‐distance propagation of coseismic ionosphere disturbances. *J. Geophys. Res.*, **2009,** 114 (A10):307.

26. Astafyeva, E., Rolland, L.M., Sladen, A. Strike-slip earthquakes can also be detected in the ionosphere. *Earth. Planet. Sci. Lett.,* **2014,** 405:180-193.

27. Astafyeva, E., Shalimov, S., Olshanskaya, E., Lognonné, P. Ionospheric response to earthquakes of different magnitudes: larger quakes perturb the ionosphere stronger and longer. *Geophys. Res. Lett.*,**2013,** 40(9):1675-1681.

28. Mokhamad Nur Cahyadi, Kosuke Heki. Coseismic ionospheric disturbance of the large strike-slip earthquakes in North Sumatra in 2012: Mw dependence of the disturbance amplitudes, *Geophysical Journal International,* **2015,** 200(1):116–129.

29. Kiratzi, A.A. Mechanism of earthquake in Aegean. *Encyclopedia of Earthquake Engineering,* **2014,**

519 4:3966.

520